ATMOSPHERIC SCIENCE

Hysteresis of the El Niño–Southern Oscillation to CO_2 forcing

Chao Liu[1], Soon-Il An[1,2,3]*, Fei-Fei Jin[4], Jongsoo Shin[3], Jong-Seong Kug[3,5], Wenjun Zhang[6,7], Malte F. Stuecker[8], Xinyi Yuan[9,10], Aoyun Xue[3], Xin Geng[3,6,7], Soong-Ki Kim[1]

El Niño–Southern Oscillation (ENSO) is the strongest interannual climate variability with far-reaching socioeconomic consequences. Many studies have investigated ENSO-projected changes under future greenhouse warming, but its responses to plausible mitigation behaviors remain unknown. We show that ENSO sea surface temperature (SST) variability and associated global teleconnection patterns exhibit strong hysteretic responses to carbon dioxide (CO_2) reduction based on the 28-member ensemble simulations of the CESM1.2 model under an idealized CO_2 ramp-up and ramp-down scenario. There is a substantial increase in the ensemble-averaged eastern Pacific SST anomaly variance during the ramp-down period compared to the ramp-up period. Such ENSO hysteresis is mainly attributed to the hysteretic response of the tropical Pacific Intertropical Convergence Zone meridional position to CO_2 removal and is further supported by several selected single-member Coupled Model Intercomparison Project Phase 6 (CMIP6) model simulations. The presence of ENSO hysteresis leads to its amplified and prolonged impact in a warming climate, depending on the details of future mitigation pathways.

INTRODUCTION

Human-induced greenhouse gas emissions, primarily in the form of carbon dioxide (CO_2), have led to an unprecedented rate of warming in the Earth's climate, raising serious concerns about emerging and impending climate change risks (*1*). One of these risks is climate hysteresis, which refers to the delayed responses of the Earth's climate system on multigenerational human scales when external forcing is restored to baseline levels. In other words, the climate system could evolve to completely different states at the same level of radiative forcing, but at different stages of the pathway (i.e., ramp-up versus ramp-down). Various idealized modeling experiments have been conducted with different approaches to perturbing or removing the transient CO_2 forcing (*2*–*5*). Several key climate elements, such as global mean surface temperature and precipitation (*5*–*8*), sea level (*3*), the Antarctic ice sheet (*9*), the Atlantic Meridional Overturning Circulation (AMOC) (*5*), and the Intertropical Convergence Zone (ITCZ) (*10*–*12*), all exhibit different degrees of hysteresis behavior. The inertial effects induced by slow ocean circulation adjustment processes are thought to be one of the main reasons (*8*).

The El Niño–Southern Oscillation (ENSO) is a natural phenomenon characterized by irregular interannual swings between warm (El Niño) and cold (La Niña) conditions over the central-to-eastern equatorial Pacific region (*13*, *14*). The concomitant changes in atmospheric winds and deep convection not only excite both positive and negative ocean-atmosphere feedbacks that promote the rapid growth and phase transition of ENSO but also effectively trigger climatic teleconnections that spread its influence across the globe (*15*–*17*). Hence, ENSO is a dominant mode of climate variability and provides a leading source of forecasting information for seasonal climate prediction (*18*). Strong changes in the properties of ENSO can therefore have serious socioeconomic consequences (*19*, *20*).

The stability and characteristics of ENSO are strongly controlled by the background mean state (*21*), which is continuously changing under anthropogenic global warming. Various aspects of ENSO characteristics, such as intensity (*22*), asymmetry (*23*), duration (*24*), spatial pattern (*25*), frequency (*26*, *27*), and teleconnections (*28*), are all projected to change in a warming climate, albeit with varying degrees of confidence in the presence of noise interference, scenario-based uncertainties, process representation, and model biases (*29*–*33*). In particular, there is a high intermodel consistency that El Niño–associated tropical Pacific precipitation will become more intense and farther east under a transient CO_2-increase scenario (*34*, *35*). Such projected changes become pronounced further as CO_2 stabilizes (*36*), suggesting the possibility of hysteresis. Nevertheless, future changes in ENSO sea surface temperature (SST) variability show less consensus and depend heavily on models, scenarios, and/or even the length of the analysis periods (*29*).

In contrast to the projected ENSO changes under global warming, which have been extensively studied, the response of ENSO to CO_2-reduction scenarios has hitherto received less attention. A comprehensive understanding of this topic will provide a reference for future ENSO changes under plausible mitigation pathways and shed light on the uncertain ENSO SST changes in

[1]Irreversible Climate Change Research Center, Yonsei University, Seodaemun-gu, Seoul 03722, Republic of Korea. [2]Department of Atmospheric Sciences, Yonsei University, Seodaemun-gu, Seoul 03722, Republic of Korea. [3]Division of Environmental Science and Engineering, Pohang University of Science and Technology (POSTECH), Pohang, Republic of Korea. [4]Department of Atmospheric Sciences, School of Ocean and Earth Science and Technology (SOEST), University of Hawai'i at Mānoa, Honolulu, HI 96822, USA. [5]Institute for Convergence Research and Education in Advanced Technology, Yonsei University, Seoul, South Korea. [6]CIC-FEMD/ILCEC, Key Laboratory of Meteorological Disaster of Ministry of Education (KLME), Nanjing University of Information Science and Technology, Nanjing 210044, China. [7]School of Atmospheric Sciences, Nanjing University of Information Science and Technology, Nanjing 210044, China. [8]Department of Oceanography & International Pacific Research Center (IPRC), School of Ocean and Earth Science and Technology (SOEST), University of Hawai'i at Mānoa, Honolulu, HI 96822, USA. [9]Key Laboratory of Transportation Meteorology, China Meteorological Administration (CMA), Nanjing 210041, China. [10]Jiangsu Meteorological Service Centre, Nanjing 210041, China.
*Corresponding author. Email: sian@yonsei.ac.kr

transient warming scenarios by comparing ENSO responses between the CO_2 ramp-up and ramp-down phases. A previous study (*37*) suggests that ENSO SST variability exhibits a hysteresis amplification to CO_2 reduction due to the delayed El Nino–like background warming. However, the detailed physical link is not well established in this study and thus deserves further investigation.

For our investigation, we conduct an idealized CO_2 ramp-up and ramp-down experiment with 28 ensemble members (see Materials and Methods) using the Community Earth System Model version 1.2 (CESM1.2) (*38*), which provides a realistic simulation of ENSO dynamics. The selected single-member Coupled Model Intercomparison Project Phase 6 (CMIP6) models (*39*) with high fidelity in representing nonlinear features of the eastern Pacific ENSO SST under similar experimental CO_2 ramp-up and ramp-down scenarios but slightly different initial CO_2 concentration levels (see Materials and Methods) are also analyzed to ensure robust results.

RESULTS

Hysteresis of ENSO SST variability and related air-sea coupling processes

We first examine the ENSO representation in the CESM1.2 model, which is the basis for the credible futuristic projection of ENSO. The variance (Fig. 1C) and skewness (fig. S1C) of the equatorial Pacific SST anomaly in the present-day (PD) control simulation, which largely encapsulates the physical processes of ENSO, are very similar to the observations (fig. S1, A and B), suggesting that this model provides a realistic simulation of ENSO. Based on this, the ENSO SST variability exhibits a prominent hysteresis response to CO_2 ramp-up and ramp-down (Fig. 1A). There is a moderate and nonmonotonic increase in the ensemble mean eastern Pacific SST variance during the CO_2 ramp-up period (for the years 2001–2140). The superimposed ensemble spread renders the increased variance indistinguishable from zero due to strong internal variability (Fig. 1B). These results are consistent with previous multimodel ensemble findings (*40*), suggesting that forced ENSO SST responses exist in a transient warming scenario, but are relatively difficult to detect.

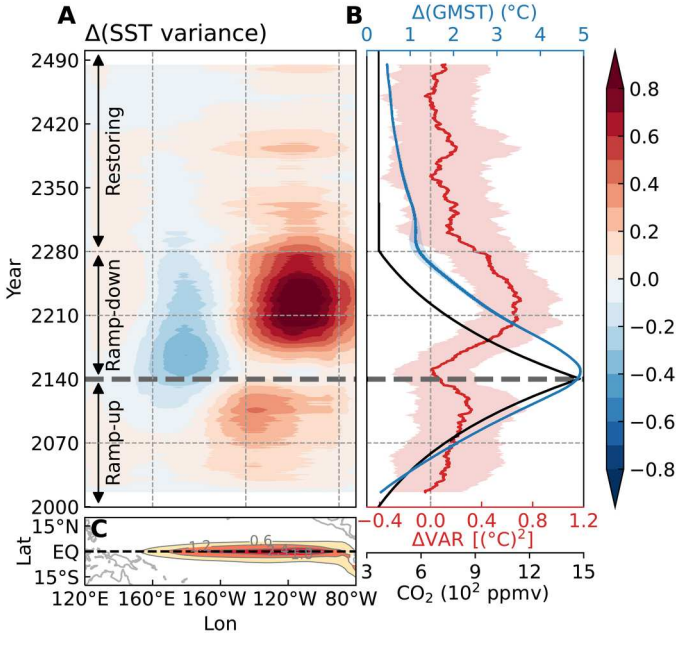

Fig. 1. Hysteresis of ENSO SST variability. CESM1.2 ensemble-averaged SST anomaly variance [unit: $(°C)^2$] in the equatorial (5°S to 5°N) Pacific [(**A**), shading] and equatorial eastern Pacific [(**B**), red line] relative to the present-day control simulation [(**C**), shading and contours]. The black solid line and blue line represent the CO_2 concentration and ensemble-averaged global mean surface temperature (GMST), respectively. The shading in (B) represents two intermember SDs spread of related physical quantities. Vertical dashed lines in (A) indicate the eastern (90°W to 145°W) and central Pacific (160°E to 145°W) regions, respectively. Horizontal dashed lines indicate different stages of CO_2 forcing. The Δ symbol indicates the ensemble-averaged change relative to the control simulation ensemble average.

Counterintuitively, ENSO activity shows exaggerated hysteretic changes when the CO_2 forcing is reduced (for the years 2141–2280). There is a strong increase in ENSO intensity in the eastern Pacific that is centered around the middle of the ramp-down period (the year 2210), along with a slightly weakened signal in the central Pacific immediately after the peak of the CO_2 forcing (Fig. 1A). In particular, under the same condition of a double CO_2 concentration compared to the PD level, the eastern Pacific SST anomaly variance increases by ~50% in the year 2210, but only by ~15% in the year 2070. Such strong hysteresis character of ENSO SST variability is distinct from the thermal inertia-induced hysteresis of global mean surface temperature, which closely follows the CO_2 forcing trajectory during the ramp-up period and lags slightly behind the CO_2 forcing by ~10 years during the ramp-down period (Fig. 1B). This implies that the ENSO hysteresis cannot be explained by thermodynamic processes alone. When the CO_2 concentration further decreases to its PD level (in the years 2281–2500), ENSO activity quickly returns to normal conditions, indicating a possibility that ENSO-related climate change can be reversed (Fig. 1, A and B).

Changes in ENSO SST variability are closely related to the time-varying strength of the equatorial air-sea coupling, which can be decomposed into several competing feedbacks using an ocean mixed-layer heat budget analysis (see Materials and Methods). Here, we separate the responses of El Niño and La Niña by considering their asymmetric dynamics and find that changes in the tropical air-sea coupling hysteresis occur mainly during the El Niño phase. Specifically, El Niño precipitation continuously increases and moves eastward until about the middle of the ramp-down period (the year 2210), showing a pronounced hysteresis feature (Fig. 2A). However, La Niña–related precipitation over the central-eastern equatorial Pacific is roughly symmetric with the CO_2 pathway and thus shows weak hysteresis changes (fig. S2A). Correspondingly, El Niño–related feedback changes show more pronounced hysteresis behavior than those during La Niña (fig. S3). The dominance of El Niño changes is also evidenced by a similar hysteresis feature in its frequency (fig. S2B), while La Niña frequency shows uncertain responses (fig. S2C).

Physically, there are similar hysteresis changes in strengthened and eastward-propagating anomalous zonal surface wind stress due to El Niño precipitation changes (Fig. 2A). Such wind strength and structural changes enhance the eastern Pacific thermocline responses and the resultant thermocline feedback (TH) by increasing the zonal-mean momentum flux input (Fig. 2A) and enhancing the wind-thermocline sensitivity (fig. S4A), respectively. Other TH-related parameters, including mean upwelling (fig. S4D) and thermocline-induced subsurface ocean temperature change (fig. S4B), exhibit unfavorable and weak hysteresis changes in the eastern

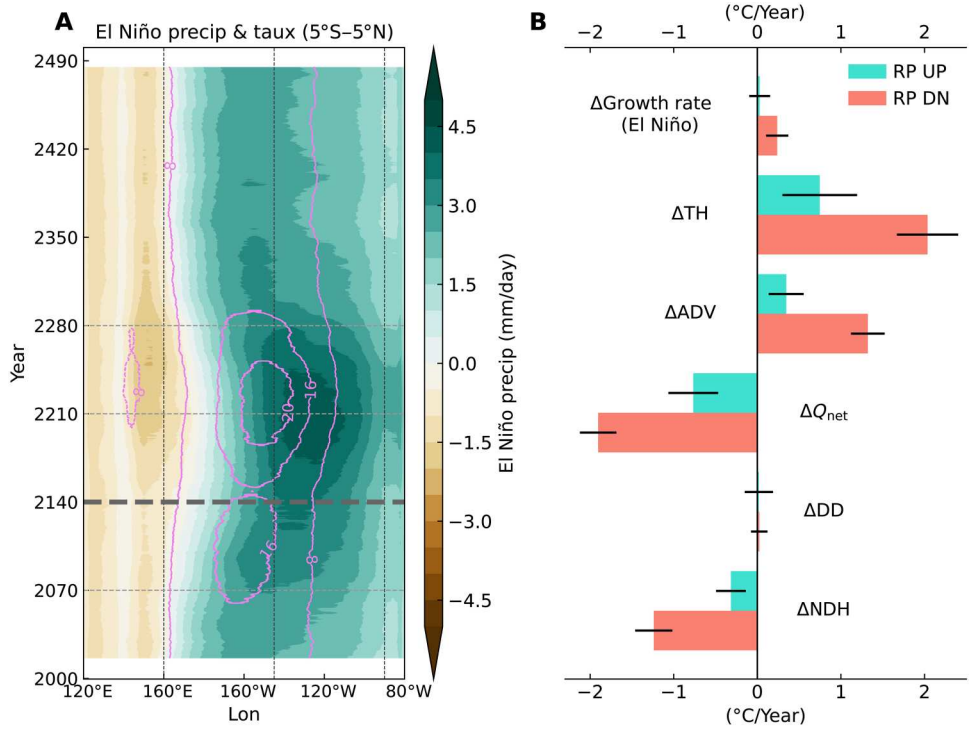

Fig. 2. Changes in El Niño–coupled processes. (**A**) CESM1.2 ensemble-averaged Hovmöller diagrams of El Niño precipitation (unit: mm/day, shading) and surface zonal wind stress (unit: 0.01 N/m^2, contours). (**B**) El Niño eastern Pacific SST anomaly growth rate changes (unit: °C/year) and different feedback contributions during the ramp-up (green) and ramp-down (red) period. TH, ADV, Q_{net}, DD, and NDH represent thermocline feedback, advective feedback, surface net heat flux, dynamical damping, and nonlinear dynamical heating, respectively. Vertical dashed lines in (A) indicate the eastern (90°W to 145°W) and central Pacific (160°E to 145°W) regions, respectively. Horizontal dashed lines in (A) indicate different stages of CO_2 forcing. The Δ symbol in (B) indicates the ensemble-averaged change relative to the control simulation ensemble average. Error bar lines in (B) represent two intermember SDs spread estimated among 31-year moving windows.

Pacific, respectively, and are thus less important. Because of a stronger wind-driven surface zonal current (fig. S4C), the advective feedback (ADV) (Fig. 2B) dominated by its zonal component also gets amplified (fig. S5). Although increased central Pacific vertical stratification (fig. S6) may also enhance the upper-ocean responses to wind forcing (*22*) and contribute to the ENSO variability hysteresis, its peak timing (~2160) is much earlier than those (~2210) of ENSO SST variance (Fig. 1, A and B) and wind-thermocline sensitivity (fig. S4A), suggesting its secondary role in determining the key hysteresis feature of ENSO. Meanwhile, the net heat flux (Q_{net}) and nonlinear dynamical heating (NDH) terms that damp El Niño SST growth also get enhanced during the ramp-down period (Fig. 2B and fig. S3, C and E), while the dynamical damping (DD) term is overall negligible in the eastern Pacific (Fig. 2B and fig. S3D). All these feedback processes collectively produce a small yet positive growth rate of the eastern Pacific SST anomaly (Fig. 2B), thus favoring the enhancement of local SST variability. We also examined the unresolved physical processes represented by the heat budget residual and found that it plays a negligible role (fig. S3F).

Mechanism of ENSO hysteresis

The strengthening and eastward-moving air-sea coupling center is particularly important for characteristic changes in El Niño. This may be subject to changes in the background state. In response to the CO_2 forcing, the eastern equatorial Pacific experiences an El Niño–like mean state change, with its maximum magnitude delayed by about two decades after the CO_2 peak due to the thermal inertia of the tropical Pacific (fig. S4, E and F). Although such background SST warming thermodynamically enhances the equatorial SST precipitation sensitivity to some extent (*34*, *35*), its peak timing (approximately the year 2160) is earlier than that of the ENSO characteristic (the year 2210), indicating indispensable roles played by other processes. In addition to the equatorial dynamics in the zonal direction, meridional physical processes, usually associated with the ITCZ, also play an important role in ENSO development and characteristic changes (*41*, *42*). Using a precipitation centroid index (see Materials and Methods), we find that the meridional position of the ITCZ shares the similar hysteresis feature of peak timing (Fig. 3A) with the El Niño characteristic changes, suggesting that they are physically linked.

The equatorial central-to-eastern Pacific region becomes wetter, while the subtropical regions in both hemispheres become drier during the ramp-up period (Fig. 3D), closely following the "warmer-get-wetter" paradigm (*43*). Because of a more severe precipitation deficit in the Northern Hemisphere, the Pacific ITCZ centroid as a whole slowly moves southward (Fig. 3A). Such ITCZ changes are particularly evident around the CO_2 peak phase (Fig. 3C). In particular, there is an eastward expansion of the South Pacific Convergence Zone (SPCZ) due to strong moistening of the near-equatorial central Pacific (Fig. 3C), which coincides with

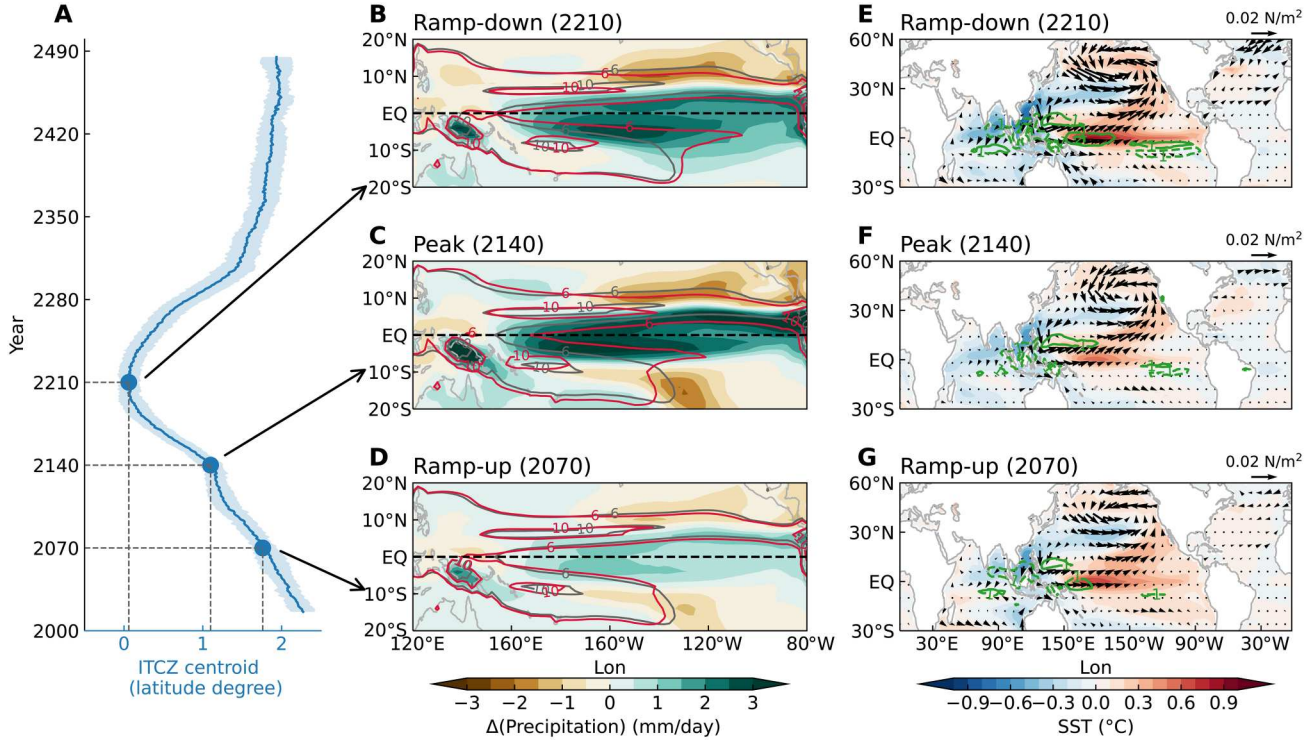

Fig. 3. Role of ITCZ hysteresis. (**A**) CESM1.2 ensemble-averaged centroid (unit: degrees latitude) of tropical Pacific (120°E to 80°W, 20°S to 20°N) zonal mean annual precipitation (blue line). Blue shading represents the two intermember SDs spread. (**B** to **D**) Background mean precipitation (unit: mm/day, red contours) and their relative changes to the CESM1.2 control simulation (shading) within a 31-year window centered at the middle of the ramp-down period (B), CO_2 peak phase (C), and the middle of the ramp-up period (D). Gray contours represent long-term mean precipitation in the control simulation. (**E** to **G**) CESM1.2 ensemble-averaged January-February-March mean SST (unit: °C, shading), precipitation (unit: mm/day, contours), and surface wind stress (unit: N/m^2, vector) anomalies regressed onto subsequent December-January-February mean El Niño SST index (180°W to 90°W, 5°S to 5°N) at the middle of the ramp-down period (E), CO_2 peak phase (F), and the middle of the ramp-up period (G).

a local increase in simultaneous SST precipitation sensitivity (Fig. 2A).

Two to three decades after the turning point of the CO_2 forcing, rainfall in both equatorial and subtropical northeast Pacific begins to recover, exhibiting weak to moderate hysteresis behavior (fig. S7). Rainfall in the subtropical southeast Pacific rebounds immediately after the CO_2 peak at more than twice the rate of the ramp-up period (fig. S7B). This contrasting interhemispheric precipitation recovery rate further accelerates the southward migration of the ITCZ and eventually brings the ITCZ centroid to the equator in 2210 (Fig. 3A). Spatially, the equatorial precipitation centroid represents an interhemispheric symmetric ITCZ structure and a more eastward-extended SPCZ than the CO_2 peak phase (Fig. 3B). The expanding SPCZ further favors El Niño occurrence by increasing the sensitivity of the eastern Pacific atmosphere to El Niño precursors during its early stages (Fig. 3, E to G). Equatorial positive feedback processes amplify these disturbances and eventually promote an eastward shift of the El Niño action center. Such ITCZ hysteresis is less affected when the ENSO rectification effect on mean precipitation changes is excluded (fig. S8). A previous study suggests that the ITCZ hysteresis is primarily due to an interhemispheric energy imbalance, which can be further attributed to the slow recovery of the AMOC and the larger heat capacity of the Southern Ocean (*5*, *11*). Since our main focus in this study is on changes in ENSO activity, we refer the reader to the two parallel studies above for the detailed physical processes behind ITCZ and AMOC hysteresis changes.

ENSO hysteresis in CMIP6 models

Aside from the large ensemble simulations of the CESM1.2 model, we also analyze eight available CMIP6 single-member model simulations under a similar CO_2 ramp-up and ramp-down scenario but with a slightly different initial CO_2 concentration level [preindustrial level, 284.7 ppmv (parts per million by volume)] to further corroborate our findings. We first use the Niño3 SST skewness as a simple touchstone to evaluate the performance of each CMIP6 model in simulating the nonlinear dynamics of ENSO (fig. S9) (*22*, *44*), considering that a realistic El Niño regime is a prerequisite for its credible future projections (*45*). Although all models reproduce seemingly reasonable SST intensities (fig. S9A), only the MIROC-ES2L and NorESM2-LM models simulate a stable positive SST skew in the eastern Pacific that mimics the observed features (fig. S9B). In these two models, changes in ENSO SST variability (Fig. 4, A and D) show consistent hysteresis features with our CESM1.2 model (Fig. 1), despite subtle differences, and thus support our CESM1.2-based findings. In the MIROC-ES2L model, the enhanced El Niño–related precipitation response in the equatorial Pacific persists almost throughout the ramp-down phase (Fig. 4B), leading to the hysteresis changes in the air-sea coupling strength and the ENSO SST variance. However, the El Niño

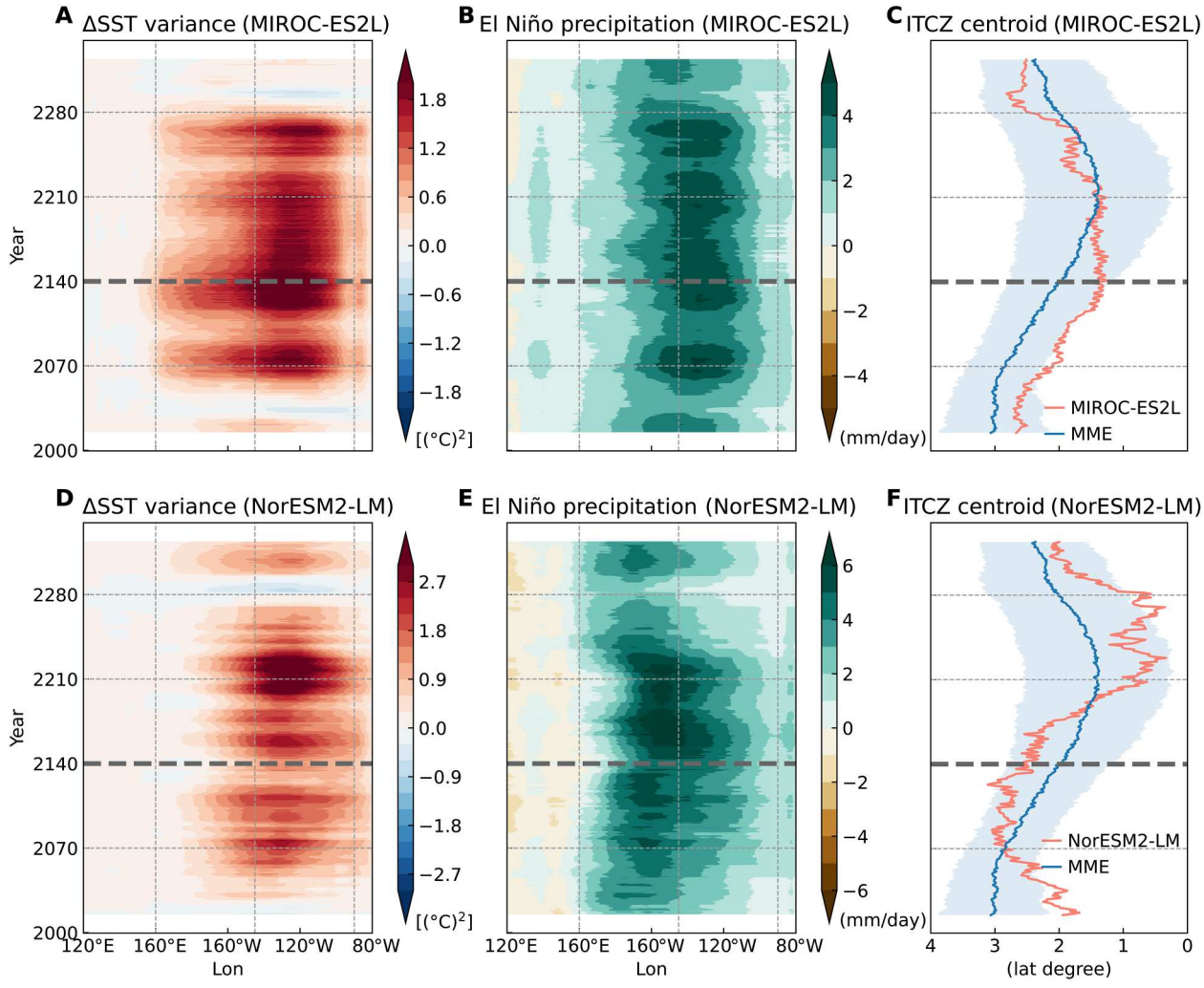

Fig. 4. ENSO hysteresis in two selected CMIP6 models. (**A** to **C**) The MIROC-ES2L model-based single-member results. Hovmöller diagrams of equatorial Pacific interannual (<8 years) SST variance [unit: $(°C)^2$] changes (A) and El Niño precipitation anomalies [unit: mm/day; (B)]. (C) Time evolution of the tropical Pacific zonal mean precipitation centroid in this model (unit: degree, red line) and the CMIP6 multimodel ensemble mean result (blue line). Light blue shading represents the corresponding two intermodel SD spreads. Vertical dashed lines in (A) and (B) indicate the eastern (90°W to 145°W) and central Pacific (160°E to 145°W) regions, respectively. Horizontal dashed lines indicate different stages of CO_2 forcing. The Δ symbol in (A) indicates the change relative to the control simulation ensemble average. (D) to (F) as (A) to (C), but for the NorESM2-LM model-based single-member results.

precipitation center exhibits near-standing features and does not propagate further eastward after the CO_2 peak phase, coinciding with a simultaneous stalled southward migration of the ITCZ (Fig. 4C), which is slightly different from the multimodel ensemble mean and the CESM1.2 model results. Another NorESM2-LM model can generally simulate the hysteresis behavior of the ITCZ position (Fig. 4F) and its resultant change in ENSO variability (Fig. 4, D and E), with some temporary discrepancies possibly due to the limited ensemble size, thus further supporting our findings.

The other six CMIP6 models that fail to reproduce the observed nonlinear El Niño regime in their control simulation show quite large intermodel diversities in future ENSO variability and hysteresis changes (fig. S10), which can be roughly grouped into three different categories. The first model group consists of the ACCESS-ESM1-5 and CanESM5 models, which simulate some hysteresis changes in SST variance (fig. S10, A and D) over the central-to-eastern equatorial Pacific and support our findings in a general sense, but their changes are either more concentrated in the central Pacific (fig. S10A) or loosely organized with weak magnitude (fig. S10D). The associated El Niño precipitation is also either much narrower (fig. S11A) or weaker (fig. S11D), both with more westward locations compared to our CESM1.2 model (Fig. 2A) and the other two selected CMIP6 models (Fig. 4, B and E), potentially limiting the strength of the air-sea coupling, the eastern Pacific SST variability, and its future changes. Thus, it is better to distinguish these degraded ENSO hysteresis behaviors owing to apparent model biases from the model results with more realistic ENSO nonlinear dynamics (i.e., CESM1.2, MIROC-ES2L, and NorESM2-LM).

The second group of models, including the CESM2 and the CNRM-ESM2-1, shows opposite hysteresis changes with larger ENSO variance in the ramp-up period than in the ramp-down

period (fig. S10, B and C). In particular, the CESM2 model shows a continuously decreasing SST variability (fig. S10B), most evident in the central Pacific, despite under the condition of an exaggerated hysteresis of the ITCZ position southward movement (fig. S12B), while the SST variance in the CNRM-ESM2-1 model first increases in the ramp-up period but shows almost diminished changes in the ramp-down period (fig. S10C). While the common model bias of the underestimated SST precipitation sensitivity (fig. S11C) may account for the distinct hysteresis behavior in the CNRM-ESM2-1, it seems less relevant in the CESM2, as it simulates stronger and more eastward-located El Niño precipitation (fig. S11B) compared to other biased models in the early stage of the ramp-up period (fig. S11, A and C to F). The GFDL-ESM4 and UKESM1-0-LL belong to the third model group but are not completely exclusive with the other two model groups, showing episodic variance changes and less clear hysteresis behavior (fig. S10, E and F). Both models also suffer from the common model bias of too narrow a zonal extent and too westward location of El Niño precipitation (fig. S11, E and F).

In a qualitative sense, all CMIP6 models simulate similar hysteresis changes in the tropical Pacific background states in terms of ITCZ southward migration (fig. S12) and El Niño–like mean state warming (fig. S13), suggesting that their contrastingly different ENSO hysteresis behaviors are arguably highly dependent on their respective representations of the basic ENSO dynamics, including the overall underestimated SST precipitation sensitivity as shown. While the eastern equatorial Pacific SST skewness metric can identify models with more realistic nonlinear ENSO dynamics, it is not sufficient to quantitatively constrain future ENSO projections due to the quite divergent ENSO hysteresis changes within the six models with weak ENSO skewness. An in-depth understanding of each model's bias and associated unique ENSO response to external forcing, such as the CESM2 model, is warranted for model improvement and credible future projections, but is beyond the scope of this study and will be explored elsewhere in the future.

Hysteresis of ENSO atmospheric teleconnections

All of the impacts associated with El Niño in a warming world can be further exacerbated in the presence of El Niño hysteresis behavior to CO_2 forcing and thus have important implications for human society. To illustrate this in a general perspective, we focus on two key climatic variables from the CESM1.2 model, namely, global land surface temperature and precipitation, and show their altered responses in the context of El Niño hysteresis (Fig. 5). The El Niño teleconnections during the ramp-down period are more vigorous with subtle regional structural changes (Fig. 5). During the El Niño peak phase (Fig. 5, A and B), two well-known atmospheric teleconnections (*46*, *47*), the Pacific-North American and Pacific-South American patterns, further strengthen and shift eastward during the ramp-down period in response to a similar zonal shift of the El Niño convective center (Fig. 2A). These changes lead to more negative surface temperature anomalies over the most continental part of North America and the midlatitude regions of South America (Fig. 5B). In particular, the intensified Aleutian Low anomaly manifested on the surface during the ramp-down phase and its associated northeasterly surface winds (fig. S14) generate more negative surface temperature anomalies over high-latitude eastern Russia, Alaska, Canada, and the North American continent (Fig. 5B) mainly through cold advection.

Downstream El Niño teleconnections are also strengthened in most tropical regions (Fig. 5, A and B). For example, the enhanced El Niño precipitation during the CO_2 ramp-down phase releases more latent heat into the atmosphere, resulting in a warmer tropical troposphere (fig. S15, A and B), which increases static stability and surface temperature anomalies in remote areas (i.e., the TT mechanism) (*48*), especially in the tropical parts of South America, North Africa, and the Indochinese Peninsula (Fig. 5B). El Niño–induced surface temperature anomalies are also enhanced in the subtropical East Asia region but attenuated over eastern Australia (Fig. 5B), both of which lie outside the warm belt of tropical tropospheric temperature anomalies (fig. S15, A and B) and thus cannot be explained by the altered TT mechanism. In these two regions, the El Niño–induced low-level circulation changes are more important. Specifically, the enhanced southerly wind anomalies to the west of the western North Pacific anticyclone during the peak El Niño winter in the ramp-down period can further weaken the East Asian winter monsoon and advect more tropical high temperature northward (fig. S15, C and D) (*49*), eventually exposing East Asia to higher temperature anomalies (Fig. 5, A and B).

The Australian region usually experiences higher surface temperature anomalies during El Niño peaks due to reduced cloud cover and increased solar radiation associated with the broad descending branch of the Walker circulation (*50*). During the CO_2 ramp-down phase, El Niño becomes stronger but more eastward shifted, resulting in small changes in the Walker circulation influence represented by the local low-level velocity potential (fig. S15, E and F). However, the concurrent enhanced low-level northerly wind anomalies to the east of the enhanced and more eastward-located anticyclonic circulation in the tropical southern Indian Ocean can advect more midlatitude low temperature southward (fig. S15, C and D), thus potentially reducing the El Niño–related positive surface temperature anomalies over eastern Australia (Fig. 5, A and B).

El Niño hysteresis also further strengthens the entire Asian-Australian monsoon system in the post–El Niño boreal summer (Fig. 5, C and D). The delayed basin-wide SST warming of the Indian Ocean and the developing La Niña SST anomalies in the equatorial Pacific are two major controlling factors for the low-level anticyclonic circulation anomalies in the western Pacific during the post-El Niño summer, both in the present and under climate change conditions (*51*–*53*). Compared to the ramp-up phase (fig. S15G), the magnitude of the Indian Ocean basin warming and the developing Pacific La Niña SST in the CO_2 ramp-down phase increase by about 30% (0.09°C) and 20% (−0.06°C), respectively (fig. S15H). The associated changes in local precipitation anomalies (fig. S15, I and J) can respectively excite stronger atmospheric Kelvin wave (*51*) and Rossby wave responses (*54*), leading to the intensification of the anticyclonic circulation anomalies in the western Pacific and ultimately elevating the flood risks in both East Asia and Austria (Fig. 5, C and D).

Briefly, most of the world's population would experience increased climate change risks for an extended period even with a reduction in CO_2 forcing. Because of limited ensemble members and severe biases of El Niño precipitation in available CMIP6 models, we here accessed the hysteresis in El Niño teleconnections only using a single CESM1.2 model, leaving the possibility of model-dependent results. While our study presents ENSO teleconnection hysteresis from a global-scale perspective, climate change

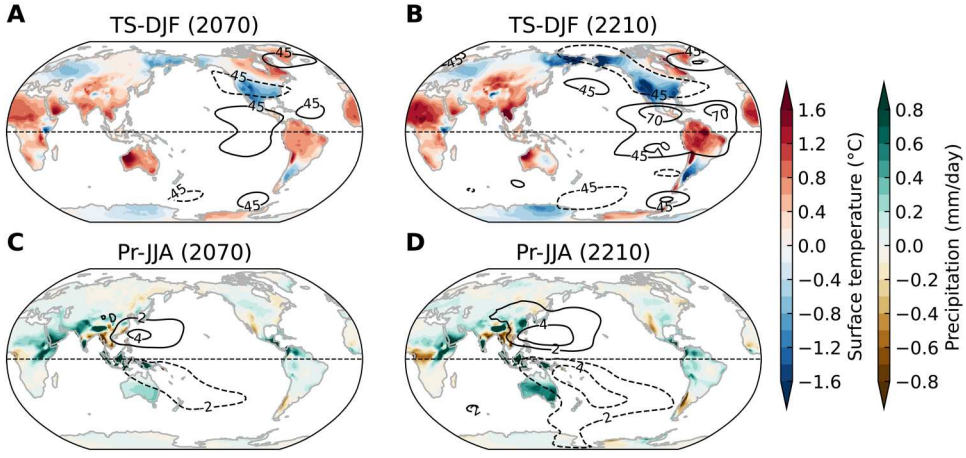

Fig. 5. Amplified El Niño teleconnections. (**A** and **B**) CESM1.2 ensemble-averaged regressed December-January-February (DJF) mean land surface temperature anomalies (unit: °C, shading) and 200 hPa geopotential height (unit: m, contours) onto the simultaneous positive phase of normalized El Niño SST anomaly index (180°W to 90°W, 5°S to 5°N) in a 31-year time window centered at the midpoint of the ramp-up [(A), 2070] and ramp-down [(B), 2210] periods. (**C** and **D**) CESM1.2 ensemble-averaged regressed June-July-August averaged land precipitation anomalies (unit: mm/day, shading) and 850 hPa stream function (unit: $10^6 m^2/s$, contours) onto the positive phase of previous DJF El Niño–normalized SST anomaly index (180°W to 90°W, 5°S to 5°N) in a 31-year time window centered at the midpoint of the ramp-up [(C), 2070] and ramp-down [(D), 2210] period.

consequences are often more perceived on a regional scale. Thus, further studies using models with improved physics and large ensemble members, more realistic experimental scenarios, and a focus on finer target regions with more comprehensive physical quantities are all needed to better quantify the mitigation costs and manage regional disasters.

DISCUSSION

In this study, we use a hypothetical carbon dioxide removal scenario to show that ENSO properties exhibit pronounced hysteresis responses to CO_2 reduction, thereby prolonging the consequential influence of ENSO globally in a warming climate. These results provide a benchmark for how ENSO would respond to changes or perturbations in CO_2 forcing and have important implications for various mitigation policies. While our CO_2 forcing followed the standard protocol endorsed by the Carbon Dioxide Removal Model Intercomparison Project (CDRMIP), the sensitivity of ENSO to the external forcing rate, the peak CO_2 concentration level, the carbon dioxide removal approaches, and, more generally, the mitigation pathways deserve further investigation.

In our study, we emphasize the hysteresis role of the background ITCZ position change, which is influenced by an interhemispheric energy imbalance due to the long adjustment time scales of extratropical processes, primarily changes in heat uptake in the AMOC and the Southern Ocean (*5*, *11*). The ITCZ, a key mediator linking tropical and extratropical changes (*55*), still suffers from a notorious systematic bias in most CMIP6 models (*56*). An authentic representation of ENSO nonlinear dynamics, a crucial prerequisite for ENSO future projections, is also missing in the majority of contemporary models (fig. S9), despite their seemingly reasonable performance in terms of SST anomaly amplitude (*44*, *45*). Therefore, we suggest that realistic model representations of ENSO dynamics, ITCZ dynamics, their interactions, and potential remote modulators are all important for both credible projections of future ENSO activity and risk assessment of various mitigation strategies.

MATERIALS AND METHODS

Experimental design and datasets

To investigate the ENSO hysteresis response to CO_2 forcing, the fully coupled CESM1.2 is used (*38*). This model comprises the atmosphere (Community Atmospheric Model version 5), ocean (Parallel Ocean Program version 2), sea ice (Community Ice Code version 4), and land models (Community Land Model version 4). The atmospheric and land components are configured with a horizontal resolution of approximately 1° and 30 vertical layers. The ocean model has 60 vertical levels, with a longitudinal resolution of 1° and a latitudinal resolution of ~0.33° near the equator, which gradually increases to 0.5° near the poles.

We design and conduct two experiments, namely, a PD control and CO_2 ramp-up and ramp-down experiments. The PD experiment is integrated for 900 years with a fixed CO_2 concentration (1× CO_2, 367 ppmv) in the present climate. The CO_2 ramp-up and ramp-down experiment branches from the PD experiment at different phases of the Pacific Decadal Oscillation and Atlantic Multidecadal Oscillation to generate a total of 28 ensemble members. Each member is forced by the same time-varying CO_2 forcing for 500 years, comprising a 1% increase per year in the CO_2 concentration for 140 years until the concentration quadrupled (4 × CO_2, 1468 ppmv, ramp-up period); and a subsequent symmetric 1% decrease per year in CO_2 concentration for another 140 years until it returned to the initial level (1 × CO_2, 367 ppmv, ramp-down period), and a fixed CO_2 concentration for the remaining 220 years (1 × CO_2, 367 ppmv, restoring period).

In addition, we use eight available models from CMIP6 (*39*): ACCESS-ESM1-5, CESM2, CNRM-ESM2-1, CanESM5, GFDL-ESM4, MIROC-ES2L, NorESM2-LM, and UKESM1-0-LL. The first 500 years of each model's preindustrial control simulation are used as a reference run, mimicking our PD experiment. The CO_2 ramp-up and ramp-down periods are replaced by the "1pctCO2" experiment from the CMIP6 Diagnostic, Evaluation, and Characterization of Klima (*39*) and the "1pctCO2-cdr" experiment from the CDRMIP (*4*), respectively. Each model has only one

ensemble member for all three experiments. The experimental setup differs slightly from our simulations, mostly in terms of the initial CO_2 concentration level (preindustrial level, 284.7 ppmv) and total simulation length. Specifically, each model is forced by the same time-varying CO_2 forcing for 340 years, comprising a 1% increase per year in the CO_2 concentration for 140 years until the concentration quadrupled (4 × CO_2, 1138.8 ppmv, ramp-up period); and a subsequent symmetric 1% decrease per year in CO_2 concentration for another 140 years until it returned to the initial level (1 × CO_2, 284.7 ppmv, ramp-down period), and a fixed CO_2 concentration for the remaining 60 years (1 × CO_2, 284.7 ppmv, restoring period).

To examine the realism of ENSO statistics in these models, the SST reanalysis dataset from the Extended Reconstructed Sea Surface Temperature, version 5 (ERSSTv5) is used (*57*). The analysis period is from 1979 to 2020 to ensure high data quality.

Definition of anomalies and data preprocessing

Anomalies are calculated relative to the climatology of the entire period for both the control run and reanalysis. A linear detrending procedure is applied to the SST reanalysis to remove the observed long-term trend. For the CO_2 ramp-up and ramp-down experiments in the CESM1.2 model, deterministic forced signals and anomalies are computed as the ensemble mean and related deviations in each member. The ENSO anomalies in each CMIP6 model are extracted with an 8-year high-pass Lanczos filter (*58*), considering that only one ensemble member is available for each model. All variables are linearly interpolated onto a common grid with 2° × 2° horizontal spatial resolution and 10-m vertical resolution in the upper ocean (down to 350-m depth).

Definition of diagnostic variables and indices

1) The thermocline depth is computed as the depth of maximum vertical temperature gradient in the equatorial Pacific upper oceans for each grid and each member.

2) The precipitation centroid is defined as the latitude that splits the annual zonal average tropical Pacific (120°E to 80°W, 20°S to 20°N) precipitation equally in half (*11*, *59*). To accurately capture the precipitation centroid, the precipitation is interpolated to a finer grid of a 0.1° increment in the meridional direction.

Mixed layer heat budget

To investigate the physical causes of the SST variance and skewness change, an ocean mixed layer heat budget analysis in partial flux form is used (*60*)

$$\frac{\partial T}{\partial t} = \frac{Q}{\rho C_p H_{\mathrm{mld}}} - \left(\frac{\partial(\overline{u}T)}{\partial x} + \frac{\partial(\overline{v}T)}{\partial y}\right) + \frac{\overline{W}T_{\mathrm{sub}}}{H_{\mathrm{mld}}} - \left(u\frac{\partial \overline{T}}{\partial x} + v\frac{\partial \overline{T}}{\partial y} + w\frac{\partial \overline{T}}{\partial z}\right) - \left(u\frac{\partial T}{\partial x} + v\frac{\partial T}{\partial y} + w\frac{\partial T}{\partial z}\right) + \varepsilon \quad (1)$$

where the variables T, u, v, and w denote the mixed-layer ocean temperature and ocean current velocities in the zonal, meridional, and vertical directions, respectively; variables with and without an overbar represent the background mean state and anomalies, respectively; T_{sub} and W are the ocean temperature anomalies and background vertical current velocity at the mixed layer base, respectively; and Q denotes the sea surface net heat flux anomalies into the ocean. The mixed layer is fixed at a depth of 50 m (H_{mld} = 50 m), while $\rho = 1026\ \mathrm{kg/m^3}$ and $C_p = 3996\ \mathrm{J/(kg\ K)}$ are the seawater density and heat capacity, respectively. The six grouped terms on the right-hand side are thermal damping by net heat flux (Q_{net}), DD by horizontal mean circulation, TH, ADV, NDH, and the sum of all unresolved physical processes (ε).

Definition of the ENSO coupling strength and its asymmetry

The ENSO SST amplitude is proportional to the net growth rate of ENSO SST anomalies, which is collectively determined by different competing feedback processes (*61*). In light of the nonnegligible asymmetry between El Niño and La Niña dynamics and their potential future changes, we estimate their time-varying SST feedback coupling strength separately by performing ENSO phase–dependent linear regressions (*62*) within a 31-year moving window

$$F = \begin{cases} a_{\mathrm{El}} \times \mathrm{SST_{ECP}} + \mathrm{resid_{El}} & (\mathrm{SST_{ECP}} > 0) \\ a_{\mathrm{La}} \times \mathrm{SST_{ECP}} + \mathrm{resid_{La}} & (\mathrm{SST_{ECP}} < 0) \end{cases} \quad (2)$$

where F and $\mathrm{SST_{ECP}}$ represent each feedback on the right-hand side of Eq. 1 and area-averaged SST anomalies over the central-to-eastern equatorial Pacific (180W° to 90°W, 5°S to 5°N) that cover ENSO's main activity center, respectively; resid represents an ENSO-unrelated feedback component that was not analyzed in our study. The "El" and "La" suffixes represent El Niño and La Niña phases, respectively. In Eq. 2, ENSO phase–dependent SST feedback coupling strengths (i.e., a_{El} and a_{La}) represent each feedback contribution to the SST linear growth rate under different ENSO phases. In each window, the $\mathrm{SST_{ECP}}$ is normalized first to avoid possible influences from time-varying changes in the ENSO intensity. This ENSO phase–dependent regression approach is also applied in the investigation of other related coupling sensitivities, such as El Niño SST and precipitation.

Supplementary Materials

This PDF file includes:

Figs. S1 to S15

REFERENCES AND NOTES

1. B. C. O'Neill, M. Oppenheimer, R. Warren, S. Hallegatte, R. E. Kopp, H. O. Pörtner, R. Scholes, J. Birkmann, W. Foden, R. Licker, K. J. Mach, P. Marbaix, M. D. Mastrandrea, J. Price, K. Takahashi, J.-P. van Ypersele, G. Yohe, IPCC reasons for concern regarding climate change risks. *Nat. Clim. Chang* **7**, 28–37 (2017).
2. C. Huntingford, J. Lowe, "Overshoot" scenarios and climate change. *Science* **316**, 829–830 (2007).
3. O. Boucher, P. R. Halloran, E. J. Burke, M. Doutriaux-Boucher, C. D. Jones, J. Lowe, M. A. Ringer, E. Robertson, P. Wu, Reversibility in an earth system model in response to CO_2 concentration changes. *Environ. Res. Lett.* **7**, 024013 (2012).
4. D. P. Keller, A. Lenton, V. Scott, N. E. Vaughan, N. Bauer, D. Ji, C. D. Jones, B. Kravitz, H. Muri, K. Zickfeld, The carbon dioxide removal model intercomparison project (CDRMIP): Rationale and experimental protocol for CMIP6. *Geosci. Model Dev.* **11**, 1133–1160 (2018).
5. S.-I. An, J. Shin, S.-W. Yeh, S.-W. Son, J.-S. Kug, S.-K. Min, H.-J. Kim, Global cooling hiatus driven by an AMOC overshoot in a carbon dioxide removal scenario. *Earths Future* **9**, e2021EF002165 (2021).
6. L. Cao, G. Bala, K. Caldeira, Why is there a short-term increase in global precipitation in response to diminished CO_2 forcing? *Geophys. Res. Lett.* **38**, L06703 (2011).
7. R. Chadwick, P. Wu, P. Good, T. Andrews, Asymmetries in tropical rainfall and circulation patterns in idealised CO_2 removal experiments. *Climate Dynam.* **40**, 295–316 (2012).

8. S.-K. Kim, J. Shin, S.-I. An, H.-J. Kim, N. Im, S.-P. Xie, J.-S. Kug, S.-W. Yeh, Widespread irreversible changes in surface temperature and precipitation in response to CO_2 forcing. *Nat. Clim. Chang.* **12**, 834–840 (2022).
9. J. Garbe, T. Albrecht, A. Levermann, J. F. Donges, R. Winkelmann, The hysteresis of the Antarctic ice sheet. *Nature* **585**, 538–544 (2020).
10. P. Wu, R. Wood, J. Ridley, J. Lowe, Temporary acceleration of the hydrological cycle in response to a CO_2 rampdown. *Geophys. Res. Lett.* **37**, L12705 (2010).
11. J.-S. Kug, J.-H. Oh, S.-I. An, S.-W. Yeh, S.-K. Min, S.-W. Son, J. Kam, Y.-G. Ham, J. Shin, Hysteresis of the intertropical convergence zone to CO_2 forcing. *Nat. Clim. Chang.* **12**, 47–53 (2021).
12. S. Zhou, P. Huang, S.-P. Xie, G. Huang, L. Wang, Varying contributions of fast and slow responses cause asymmetric tropical rainfall change between CO_2 ramp-up and ramp-down. *Sci. Bull. (Beijing).* **67**, 1702–1711 (2022).
13. J. Bjerknes, Atmospheric teleconnections from the equatorial Pacific. *Mon. Weather Rev.* **97**, 163–172 (1969).
14. M. J. McPhaden, S. E. Zebiak, M. H. Glantz, ENSO as an integrating concept in Earth science. *Science* **314**, 1740–1745 (2006).
15. J. D. Neelin, D. S. Battisti, A. C. Hirst, F.-F. Jin, Y. Wakata, T. Yamagata, S. E. Zebiak, ENSO theory. *J. Geophys. Res. Oceans* **103**, 14261–14290 (1998).
16. K. E. Trenberth, G. W. Branstator, D. Karoly, A. Kumar, N.-C. Lau, C. Ropelewski, Progress during TOGA in understanding and modeling global teleconnections associated with tropical sea surface temperatures. *J. Geophys. Res. Oceans* **103**, 14291–14324 (1998).
17. A. S. Taschetto, C. C. Ummenhofer, M. F. Stuecker, D. Dommenget, K. Ashok, R. R. Rodrigues, S.-W. Yeh, ENSO atmospheric teleconnections, in *El Niño Southern Oscillation in a Changing Climate* (American Geophysical Union, 2020), pp. 309–335.
18. G. A. Meehl, J. H. Richter, H. Teng, A. Capotondi, K. Cobb, F. Doblas-Reyes, M. G. Donat, M. H. England, J. C. Fyfe, W. Han, H. Kim, B. P. Kirtman, Y. Kushnir, N. S. Lovenduski, M. E. Mann, W. J. Merryfield, V. Nieves, K. Pegion, N. Rosenbloom, S. C. Sanchez, A. A. Scaife, D. Smith, A. C. Subramanian, L. Sun, D. Thompson, C. C. Ummenhofer, S.-P. Xie, Initialized Earth system prediction from subseasonal to decadal timescales. *Nat. Rev. Earth Environ.* **2**, 340–357 (2021).
19. M. Latif, N. S. Keenlyside, El Niño/Southern Oscillation response to global warming. *Proc. Natl. Acad. Sci. U.S.A.* **106**, 20578–20583 (2009).
20. C. W. Callahan, J. S. Mankin, Persistent effect of El Niño on global economic growth. *Science* **380**, 1064–1069 (2023).
21. K. B. Rodgers, S.-S. Lee, N. Rosenbloom, A. Timmermann, G. Danabasoglu, C. Deser, J. Edwards, J.-E. Kim, I. R. Simpson, K. Stein, M. F. Stuecker, R. Yamaguchi, T. Bódai, E.-S. Chung, L. Huang, W. M. Kim, J.-F. Lamarque, D. L. Lombardozzi, W. R. Wieder, S. G. Yeager, Ubiquity of human-induced changes in climate variability. *Earth Syst. Dynam.* **12**, 1393–1411 (2021).
22. W. Cai, G. Wang, B. Dewitte, L. Wu, A. Santoso, K. Takahashi, Y. Yang, A. Carréric, M. J. McPhaden, Increased variability of eastern Pacific El Niño under greenhouse warming. *Nature* **564**, 201–206 (2018).
23. Y.-G. Ham, A reduction in the asymmetry of ENSO amplitude due to global warming: The role of atmospheric feedback. *Geophys. Res. Lett.* **44**, 8576–8584 (2017).
24. H. Lopez, S.-K. Lee, D. Kim, A. T. Wittenberg, S.-W. Yeh, Projections of faster onset and slower decay of El Niño in the 21st century. *Nat. Commun.* **13**, 1915 (2022).
25. S.-W. Yeh, J.-S. Kug, B. Dewitte, M.-H. Kwon, B. P. Kirtman, F.-F. Jin, El Niño in a changing climate. *Nature* **461**, 511–514 (2009).
26. W. Cai, S. Borlace, M. Lengaigne, P. van Rensch, M. Collins, G. Vecchi, A. Timmermann, A. Santoso, M. J. McPhaden, L. Wu, M. H. England, G. Wang, E. Guilyardi, F.-F. Jin, Increasing frequency of extreme El Niño events due to greenhouse warming. *Nat. Clim. Chang.* **4**, 111–116 (2014).
27. W. Cai, G. Wang, A. Santoso, M. J. McPhaden, L. Wu, F.-F. Jin, A. Timmermann, M. Collins, G. Vecchi, M. Lengaigne, M. H. England, D. Dommenget, K. Takahashi, E. Guilyardi, Increased frequency of extreme La Niña events under greenhouse warming. *Nat. Clim. Chang.* **5**, 132–137 (2015).
28. S. McGregor, C. Cassou, Y. Kosaka, A. S. Phillips, Projected ENSO teleconnection changes in CMIP6. *Geophys. Res. Lett.* **49**, e2021GL097511 (2022).
29. W. Cai, A. Santoso, M. Collins, B. Dewitte, C. Karamperidou, J.-S. Kug, M. Lengaigne, M. J. McPhaden, M. F. Stuecker, A. S. Taschetto, A. Timmermann, L. Wu, S.-W. Yeh, G. Wang, B. Ng, F. Jia, Y. Yang, J. Ying, X.-T. Zheng, T. Bayr, J. R. Brown, A. Capotondi, K. M. Cobb, B. Gan, T. Geng, Y.-G. Ham, F.-F. Jin, H.-S. Jo, X. Li, X. Lin, S. McGregor, J.-H. Park, K. Stein, K. Yang, L. Zhang, W. Zhong, Changing El Niño–Southern Oscillation in a warming climate. *Nat. Rev. Earth Environ.* **2**, 628–644 (2021).
30. C. Wengel, S.-S. Lee, M. F. Stuecker, A. Timmermann, J.-E. Chu, F. Schloesser, Future high-resolution El Niño/Southern Oscillation dynamics. *Nat. Clim. Chang.* **11**, 758–765 (2021).
31. W. Cai, B. Ng, G. Wang, A. Santoso, L. Wu, K. Yang, Increased ENSO sea surface temperature variability under four IPCC emission scenarios. *Nat. Clim. Chang.* **12**, 228–231 (2022).
32. V. Masson-Delmotte, P. Zhai, A. Pirani, S. L. Connors, C. Péan, S. Berger, N. Caud, Y. Chen, L. Goldfarb, M. I. Gomis, M. Huang, K. Leitzell, E. Lonnoy, J. B, R. Matthews, T. K. Maycock, T. Waterfield, O. Yelekçi, R. Yu, B. Zhou (Eds.) *Climate Change 2021: The Physical Science Basis. Contribution of Working Group I to the Sixth Assessment Report of the Intergovernmental Panel on Climate Change*, *2* (Cambridge Univ. Press, 2021).
33. C. W. Callahan, C. Chen, M. Rugenstein, J. Bloch-Johnson, S. Yang, E. J. Moyer, Robust decrease in El Niño/Southern Oscillation amplitude under long-term warming. *Nat. Clim. Chang.* **11**, 752–757 (2021).
34. P. Huang, S.-P. Xie, Mechanisms of change in ENSO-induced tropical Pacific rainfall variability in a warming climate. *Nat. Geosci.* **8**, 922–926 (2015).
35. Z. Yan, B. Wu, T. Li, M. Collins, R. Clark, T. Zhou, J. Murphy, G. Tan, Eastward shift and extension of ENSO-induced tropical precipitation anomalies under global warming. *Sci. Adv.* **6**, eaax4177 (2020).
36. G. Wang, W. Cai, B. Gan, L. Wu, A. Santoso, X. Lin, Z. Chen, M. J. McPhaden, Continued increase of extreme El Niño frequency long after 1.5°C warming stabilization. *Nat. Clim. Chang.* **7**, 568–572 (2017).
37. M. Ohba, J. Tsutsui, D. Nohara, Statistical parameterization expressing ENSO variability and reversibility in response to CO_2 concentration changes. *J. Climate* **27**, 398–410 (2014).
38. J. W. Hurrell, M. M. Holland, P. R. Gent, S. Ghan, J. E. Kay, P. J. Kushner, J.-F. Lamarque, W. G. Large, D. Lawrence, K. Lindsay, W. H. Lipscomb, M. C. Long, N. Mahowald, D. R. Marsh, R. B. Neale, P. Rasch, S. Vavrus, M. Vertenstein, D. Bader, W. D. Collins, J. J. Hack, J. Kiehl, S. Marshall, The community earth system model: A framework for collaborative research. *Bull. Am. Meteorol. Soc.* **94**, 1339–1360 (2013).
39. V. Eyring, S. Bony, G. A. Meehl, C. A. Senior, B. Stevens, R. J. Stouffer, K. E. Taylor, Overview of the Coupled Model Intercomparison Project Phase 6 (CMIP6) experimental design and organization. *Geosci. Model Dev.* **9**, 1937–1958 (2016).
40. S. T. Kim, W. Cai, F.-F. Jin, A. Santoso, L. Wu, E. Guilyardi, S.-I. An, Response of El Niño sea surface temperature variability to greenhouse warming. *Nat. Clim. Chang.* **4**, 786–790 (2014).
41. P. Chang, L. Zhang, R. Saravanan, D. J. Vimont, J. C. H. Chiang, L. Ji, H. Seidel, M. K. Tippett, Pacific meridional mode and El Niño—Southern Oscillation. *Geophys. Res. Lett.* **34**, L16608 (2007).
42. S. Hu, A. V. Fedorov, Cross-equatorial winds control El Niño diversity and change. *Nat. Clim. Chang.* **8**, 798–802 (2018).
43. S.-P. Xie, C. Deser, G. A. Vecchi, J. Ma, H. Teng, A. T. Wittenberg, Global warming pattern formation: Sea surface temperature and rainfall. *J. Climate* **23**, 966–986 (2010).
44. M. Hayashi, F.-F. Jin, M. F. Stuecker, Dynamics for El Niño-La Niña asymmetry constrain equatorial-Pacific warming pattern. *Nat. Commun.* **11**, 4230 (2020).
45. C. Karamperidou, F.-F. Jin, J. L. Conroy, The importance of ENSO nonlinearities in tropical pacific response to external forcing. *Climate Dynam.* **49**, 2695–2704 (2016).
46. J. M. Wallace, D. S. Gutzler, Teleconnections in the geopotential height field during the Northern Hemisphere winter. *Mon. Weather Rev.* **109**, 784–812 (1981).
47. K. C. Mo, M. Ghil, Statistics and dynamics of persistent anomalies. *J. Atmos. Sci.* **44**, 877–902 (1987).
48. J. C. H. Chiang, A. H. Sobel, Tropical tropospheric temperature variations caused by ENSO and their influence on the remote tropical climate. *J. Climate* **15**, 2616–2631 (2002).
49. X. Geng, W. Zhang, M. F. Stuecker, P. Liu, F.-F. Jin, G. Tan, Decadal modulation of the ENSO–East Asian winter monsoon relationship by the Atlantic Multidecadal Oscillation. *Climate Dynam.* **49**, 2531–2544 (2017).
50. S. Power, T. Casey, C. Folland, A. Colman, V. Mehta, Inter-decadal modulation of the impact of ENSO on Australia. *Climate Dynam.* **15**, 319–324 (1999).
51. S.-P. Xie, K. Hu, J. Hafner, H. Tokinaga, Y. Du, G. Huang, T. Sampe, Indian ocean capacitor effect on Indo–Western Pacific climate during the summer following El Niño. *J. Climate* **22**, 730–747 (2009).
52. B. Wang, B. Xiang, J.-Y. Lee, Subtropical high predictability establishes a promising way for monsoon and tropical storm predictions. *Proc. Natl. Acad. Sci. U.S.A.* **110**, 2718–2722 (2013).
53. K. Yang, W. Cai, G. Huang, K. Hu, B. Ng, G. Wang, Increased variability of the western Pacific subtropical high under greenhouse warming. *Proc. Natl. Acad. Sci. U.S.A.* **119**, e2120335119 (2022).
54. B. Wang, R. Wu, X. Fu, Pacific–East Asian teleconnection: How does ENSO affect East Asian climate? *J. Climate* **13**, 1517–1536 (2000).
55. M. F. Stuecker, A. Timmermann, F.-F. Jin, C. Proistosescu, S. M. Kang, D. Kim, K.-S. Yun, E.-S. Chung, J.-E. Chu, C. M. Bitz, K. C. Armour, M. Hayashi, Strong remote control of future equatorial warming by off-equatorial forcing. *Nat. Clim. Chang.* **10**, 124–129 (2020).
56. B. Tian, X. Dong, The double-ITCZ bias in CMIP3, CMIP5, and CMIP6 models based on annual mean precipitation. *Geophys. Res. Lett.* **47**, e2020GL087232 (2020).
57. B. Huang, P. W. Thorne, V. F. Banzon, T. Boyer, G. Chepurin, J. H. Lawrimore, M. J. Menne, T. M. Smith, R. S. Vose, H.-M. Zhang, Extended reconstructed sea surface temperature,

version 5 (ERSSTv5): Upgrades, validations, and intercomparisons. *J. Climate* **30**, 8179–8205 (2017).
58. C. E. Duchon, Lanczos filtering in one and two dimensions. *J. Appl. Meteorol.* **18**, 1016–1022 (1979).
59. D. M. W. Frierson, Y.-T. Hwang, Extratropical influence on ITCZ shifts in slab ocean simulations of global warming. *J. Climate* **25**, 720–733 (2012).
60. S.-I. An, F.-F. Jin, I.-S. Kang, The role of zonal advection feedback in phase transition and growth of ENSO in the Cane-Zebiak model. *J. Meteorol. Soc. Jpn. Ser.* **77**, 1151–1160 (1999).
61. F.-F. Jin, S. T. Kim, L. Bejarano, A coupled-stability index for ENSO. *Geophys. Res. Lett.* **33**, L23708 (2006).
62. C. Frankignoul, Y. Kwon, On the statistical estimation of asymmetrical relationship between two climate variables. *Geophys. Res. Lett.* **49**, e2022GL100777 (2022).

Acknowledgments: We would like to acknowledge the World Climate Research Programme, which, through its Working Group on Coupled Modelling, coordinated and promoted CMIP6. We thank the climate modeling groups for producing and making their model outputs available, the Earth System Grid Federation (ESGF) for archiving the data and providing access, and the multiple funding agencies that support CMIP6 and ESGF. **Funding:** This work was supported by a National Research Foundation of Korea (NRF) grant funded by the Korean government (MSIT) (NRF-2018R1A5A1024958). Model simulation and data transfer are supported by the National Supercomputing Center with supercomputing resources including technical support (KSC-2021-CHA-0030), the National Center for Meteorological Supercomputer of the Korea Meteorological Administration (KMA), and the Korea Research Environment Open NETwork (KREONET), respectively. MFS was supported by the NSF grant AGS-2141728. This is an IPRC publication 1600 and SOEST contribution 11684. X.Y. was supported by the National Natural Science Foundation of China (42205052). **Author contributions:** Conceptualization: C.L., S.-I.A., and F.-F.J. Methodology: C.L., S.-I.A., F.-F.J., and J.S. Investigation: C.L. and J.S. Visualization: C.L. Supervision: S.-I.A. and F.-F.J. Writing—original draft: C.L., S.-I.A., and M.F.S. Writing—review and editing: C.L., S.-I.A., F.-F.J., J.S., J.-S.K., W.Z., M.F.S., X.Y., A.X., X.G., and S.-K.K. **Competing interests:** The authors declare that they have no competing interests. **Data and materials availability:** All data needed to evaluate the conclusions in the paper are present in the paper and/or the Supplementary Materials. The CESM1.2 model data used in this study are available at https://figshare.com/s/060ffa53b0813a3a26e2. The CMIP6 archives and ERSSTv5 reanalysis are freely available on https://esgf-node.llnl.gov/projects/cmip6 and https://psl.noaa.gov/data/gridded/data.noaa.ersst.v5.html, respectively.

Submitted 17 March 2023
Accepted 29 June 2023
Published 2 August 2023
10.1126/sciadv.adh8442